JOM, Vol. 72, No. 12, 2020
https://doi.org/10.1007/s11837-020-04447-3
© 2020 The Minerals, Metals & Materials Society

MESOSCALE MATERIALS SCIENCE

Development of Recrystallization Texture in Commercially Pure Titanium: Experiments and Simulation

GYAN SHANKAR,[1] SREENIVAS RAGURAMAN,[1]
LUIS A. BARRALES-MORA,[2] and S. SUWAS[1,3]

1.—Department of Materials Engineering, Indian Institute of Science, Bangalore 560012, India. 2.—George W. Woodruff School of Mechanical Engineering, Georgia Institute of Technology, 2 Rue Marconi, 57070 Metz, France. 3.—e-mail: satyamsuwas@iisc.ac.in

The recrystallization behaviour of cold-rolled (CR) commercially pure (cp)-titanium was investigated by experiments and simulations. The recrystallization texture in cp-titanium depends upon the deformation texture. The main texture components of the lower deformed (50% CR) material are $\{1014\} < 2131 >$, $\{1013\} < 2131 >$ and$\{1235\} < 2311 >$, all having weak intensity, and in the case of 70% cold rolling the texture component is $\{1013\} < 3031 >$. For the simulations, a parallel 3D cellular automata (CA) model for recrystallization was employed. The simulation results showed good agreement with the recrystallization kinetics, grain size distribution, microstructure and texture. The mechanism of recrystallization and the evolution of recrystallization texture were found to depend on the site of nucleation, i.e., whether it is formed at grain boundaries, within the grain, in the lath region or in the highly deformed region such as shear bands.

INTRODUCTION

Commercially pure Ti (CP-Ti) is a promising material in biomedical applications because of its good biocompatibility and high corrosion resistance. It is also used as a structural material in aerospace and marine applications and chemical plants because of its high strength-to-weight ratio. Moreover, it appears to be a model hexagonal closed packed (HCP) material to examine the various aspects of HCP materials with a less than ideal axial ratio (c/a). Due to the above-mentioned attributes, the study deformation and recrystallization behaviour of cp-titanium are very important, as these processes constitute important parts of the overall shape making. An important outcome of the deformation and recrystallization processes is the evolution of the crystallographic texture. Due to the large dependence of the mechanical properties on texture, it is imperative to understand the evolution of recrystallization texture. Opinions in the literature vary with regard to the mechanisms that control the evolution of recrystallization texture in titanium. The typical deformation texture reported in cp-titanium has $\{2115\} < 0110 >$ as the major component, and the typical recrystallization texture comprises the $\{1013\} < 1210 >$ component.[1–5] Bozzolo et al.[2] suggested that the recrystallization texture in titanium develops from the deformation texture $\{2115\} < 0110 >$ by 30° rotation about the c-axis. It has been suggested that the component $\{1013\} < 1210 >$ of recrystallization texture is formed from the $\{2115\} < 0110 >$ component by subgrain coalescence[6] or by subgrain growth followed by oriented growth.[7–9] It has also been reported that appreciable development of the $\{1013\} < 1210 >$ texture component occurs after recrystallization during the grain growth stage.[6,10–13] Several other researchers also suggested that the texture development during annealing of cp-titanium is influenced primarily by the deformation texture[1–4,14,15]; however, there is no unique agreement regarding the mechanism.

Several studies indicate that the recrystallization texture directly depends upon the rate of deformation and annealing temperature.[16–23] Based on the annealing temperature, the recrystallization

(Received September 12, 2020; accepted October 12, 2020;
published online November 5, 2020)

texture can be divided into three categories.[24] When the annealing temperature is ≤ 500°C, the dominant components of the recrystallization texture are {2115} < 1210 > and {0001} < 1010 >, ± 30° of transverse direction (TD) splitting, which is similar to the rolling texture. Furthermore, if the annealing temperature is between 500°C and 700°C, besides complete recrystallization, some grain growth occurs leading to a recrystallization texture consisting of the components {0001} < 1210 > and {0001} < 1010 >, ± 30º to TD. When the annealing temperature is > 700°C, substantial grain growth occurs, and the recrystallization texture consists of either {1013} < 1210 > or {2025} < 1210 > components. These components manifest as ± 30º spread across the TD line on the (0001) pole figure.[24] Some other researchers[3] have shown that after cold rolling, the texture component {1125} < 1100 > develops, and after annealing, the main recrystallization texture component {1013} < 5230 > develops and gets stronger with an increase in annealing time at the expense of the {1125} < 1123 > component of the cold-rolled texture, which is in line with the findings of Bozzolo et al.[2] Zhu et al.[25] have also reported a similar course of texture evolution.

Attempts have been made to understand the effect of the mode of rolling on the development of recrystallization texture in differently rolled pure titanium.[26] For instance, the {1013} < 1230 > recrystallization texture component was developed during the recrystallization of both straight and cross-rolled cp-titanium samples. At low temperature annealing, the recrystallization texture was different in both cases. The {0225} < 2130 > recrystallization texture component was found in the unidirectionally rolled sample while the cross-rolled sample retained the initial rolling texture components.[6,15,18–23,27]

Simulation of recrystallization behaviour in titanium has also been explored by many researchers.[28,29] Chun et al.[30] carried out Monte Carlo simulation of recrystallization of cp-titanium and revealed the activation of the oriented nucleation mechanism and hence the mechanism of texture evolution. The other relevant study was carried out by Contieri et al.,[31] who simulated the recrystallization behaviour using cellular automata. However, this paper does not deal with texture prediction, and the study primarily focused on the simulation of recrystallization kinetics or grain growth. The simulation of development of the recrystallization texture in cp-titanium with different initial deformation textures has hardly been reported.

In the present study, the study of recrystallization behaviour of titanium has been investigated in a comprehensive manner including the development of the recrystallization texture through experiments and simulations. Two different initial textures (resulting from different levels of deformation) have been used as input for recrystallization texture modelling. Moreover, the different deformation levels of the initial material (prior to recrystallization) lead to different values of dislocation densities, hence different stored energies, which is also an input to the model. The simulations were carried out using a cellular automaton model.

MATERIALS AND METHODS

Experimental

Material Chemistry and Processing

Commercially pure titanium of 99.98% purity was taken in the form of a hot-rolled plate with 5 mm thickness. The plate was then annealed at 800°C for 4 h and cooled slowly to get a homogenised strain-free equiaxed grains. The material obtained after this stage was treated as the initial material. The initial material was subjected to unidirectional cold rolling for two different thickness reductions, namely 50% (true strain = – 0.69) and 70% (true strain = – 1.2). Strain per pass was equivalent to 0.05 and was kept constant in each pass. The samples from each of the sheets were annealed isothermally at 650°C for 30, 60, 90, 105, 120, 150, 180, 240 and 300 s followed by air cooling. The annealing time was chosen such that the different stages of recrystallization and grain growth could be captured.

Characterization Techniques

All the specimens were metallographically polished followed by electro-polishing using a Struers LectroPol-5 electropolisher on both normal and transverse planes. The microstructures were characterized using a field emission-scanning electron microscope (FE-SEM). EBSD measurements were carried out on the transverse plane (RD-ND) of the samples in a Helios NanoLab dual-beam field emission-scanning electron microscope (FE-SEM) equipped with an electron back-scattered diffraction (EBSD) system. The SEM was operated at 25 kV, and a step size of 200 nm was used for all the samples for EBSD scans. EBSD mappings and data analysis were carried out using the TSL OIM 8.1 software. Subdivision of EBSD mappings into subsets containing only non-recrystallized (non-RX) or recrystallized (RX) grains was done using the grain orientation spread (GOS) value. The threshold GOS value for subdivision was chosen as RX < 1.5 < non-RX.[35] Grains containing fewer than eight EBSD data points were disregarded.

Bulk texture measurements were carried out for all the samples using an x-ray texture goniometer (Rigaku x-ray diffractometer) with Co K_α radiation based on the Schulz reflection method. The measurements were performed at the mid-thickness sections of the samples. Six incomplete pole figures (α = 0–75°) were measured from the (0002), (10–10), (10–11), (10–12), (10–13) and (11–20) peaks on the rolling plane of the samples. Threedimensional orientation distribution functions (ODFs) were calculated using the MTEX software.[32–34] The TSL OIM 8.1 software was also utilized to calculate the orientation distribution functions (ODFs).

Micro-hardness testing was performed using a FM-810 micro-hardness tester on the transverse cross section of all the samples. A load of 0.98 N and 10 s dwell time were used during measurement for all the samples. Ten indents per sample were measured that were then averaged into a hardness value HV (t) at any time t. The hardness data were the used to calculate the recrystallized volume fraction, X, following the equation:[35]

$$X = \frac{HV_{initial} - HV(t)}{HV_{initial} - HV_{final}} \tag{1}$$

where HV_{initial}, HV_{final} and HV(t) denote the hardness of cold-rolled, completely recrystallized samples and at a given annealing time, t, respectively.

Simulations

To study the formation of the recrystallization texture, computer simulations were performed by means of a parallel cellular automaton (CA).[35–37] The experimentally determined deformation texture through EBSD data was used as an input to the simulation. Grain orientation spread (GOS) values obtained from TSL OIM software were used to differentiate the difference in stored energy in different orientations after deformation. The overall dislocation density of the materials after deformation was calculated using convolutional multiple whole profile fitting (CMWP) of the x-ray diffraction pattern.[38] It was used to scale the GOS value of different orientations to an effective dislocation density, which was then used as an input to CA simulation. The current CA model considers a front-tracking approach,[36] where recrystallization proceeds gradually by high-angle grain boundary migration.

For the simulations, a synthetic microstructure was generated using the in-house software MicroGen developed at the IMM, RWTH-Aachen.[36] This software utilizes experimentally determined grain size, texture, orientation-dependent dislocation densities and information on the recrystallization nuclei to approximate the deformation microstructure prior to recrystallization. Upon completion of the synthesis process, the CA domain comprised a total of 800^3 cells distributed into 5000 deformed grains. Each cell represented a volume of $(0.365\ \mu\mathrm{m})^3$ for the simulation of the 50% rolled sample and $(0.218\ \mu\mathrm{m})^3$ for the sampled rolled 70%. The CA model is essentially a pure growth model that requires a separate nucleation model. Here, modelling of the nucleation process was based on experimental observations during incipient recrystallization. In this contribution, different nucleation mechanisms such as grain boundary nucleation, shear band nucleation and recrystallization twinning were studied. At grain boundaries, the nuclei had slightly misoriented orientations, typically 5°–10°, in relation to the parent grains.[35] Thus, in the simulations the orientations of the nuclei placed at grain boundaries deviated from those of the parent grain by a value randomly chosen between 5° and 10°. For nuclei inside the grains (bulk mechanism), the orientations of nuclei were sampled from those determined experimentally (Fig. 2).

Based on the assumption that the nucleation rate scales with the dislocation density difference, we defined a nucleation efficiency ε_i with which the N_{total} nuclei were partitioned onto each grain boundary i:

$$N_i = N_{total} . \varepsilon_i = N_{total} \frac{(|\rho_{Ga} - \rho_{Gb}|)_i A_i}{\sum_i^n \left[(|\rho_{Ga} - \rho_{Gb}|)_i A_i\right]} \tag{2}$$

where A_i denotes the number of cells discretely constructing a particular grain boundary face. N_i defines the number of nuclei that are placed at a grain boundary i. The dislocation density difference is quantified by $\rho_{Ga} - \rho_{Gb}$ (the indices Ga and Gb refer to neighbouring grains of i). It is noted that the efficiency ε_i considers the number of cells associated with a specific grain boundary. It was further assumed that nucleation was restricted to high-angle grain boundaries. The grain boundary energy (γ) value 0.4 $\mathrm{J/m^2}$ and the mobility (m_{gb}) value $3 \times 10^{-11}\ \mathrm{m^4 J^{-1} s^{-1}}$[29,39,40] were used during nucleus growth simulation. For low-angle grain boundaries ($< 15°$), m_{gb} value $3.6 \times 10^{-17}\ \mathrm{m^4 J^{-1} s^{-1}}$ was used.

EXPERIMENTAL RESULTS

Microstructure and Texture of the Initial and Deformed Materials

Figure 1a–d represents the secondary electron (SE) micrographs for the initial and the cold-rolled materials. Figure 1a shows the SEM micrograph of the initial sample, which is characterized by a uniform equiaxed grain size of 50 ± 8 μm. Figure 1-b and d shows the SEM micrographs of 50% cold-rolled (CR) and 70% CR samples, respectively. The micrograph of the 50% CR samples displays some elongated grains, lath type morphology within some grains (yellow circles) and a few deformation twins (red circles). Highly deformed banded regions could be identified (green circle). The thickness of elongated grains has been measured to about 4–5 μm. The microstructure of the 70% CR sample also displays elongated grains of 1–2 μm thickness, a few deformation twins and a large highly deformed region.

Figure 2a–c shows the inverse pole figure (IPF) map of the initial, 50% CR and 70% CR samples. Laths and deformation twins in deformed grains can be easily identified in both cases. The deformation twins found in the 50% CR sample are of the compression type, which corresponds to a 64.3°/ $< -1100 >$ misorientation across the grain. The 50% CR samples also showed a confined shear band as indicated by the white arrow. Twinning occurs at the lower levels of deformation, and with the progress of deformation, twinning ceases and many dislocations form, which ultimately collapse to form shear bands. On further deformation, after 70% rolling, the dislocation density became so high that a large area of highly deformed grains (green circle) could not be indexed.

Figure 3a shows the (0001) pole figure of the initial sample. The orientations are spread all along the TD and ± 20º to TD, having a peak intensity at $\{0001\} < 1230 >$, $\{1101\} < 0110 >$ and $\{3211\} < 0110 >$. Figure 3b shows the (0001) pole figure of the 50% CR sample. All the orientations appear to be confined toward the basal orientation. A closer view shows that the texture is comprised of a near basal fibre with a 15°–18° spread along the TD and 8°–10° spread along the RD. It should be noted that this is not a very usual deformation texture of titanium because a complete TD split did not occur owing to the relatively low deformation. Figure 3f shows the (0001) pole figure of the 70% CR sample. A typical TD split by 25°–30° having a

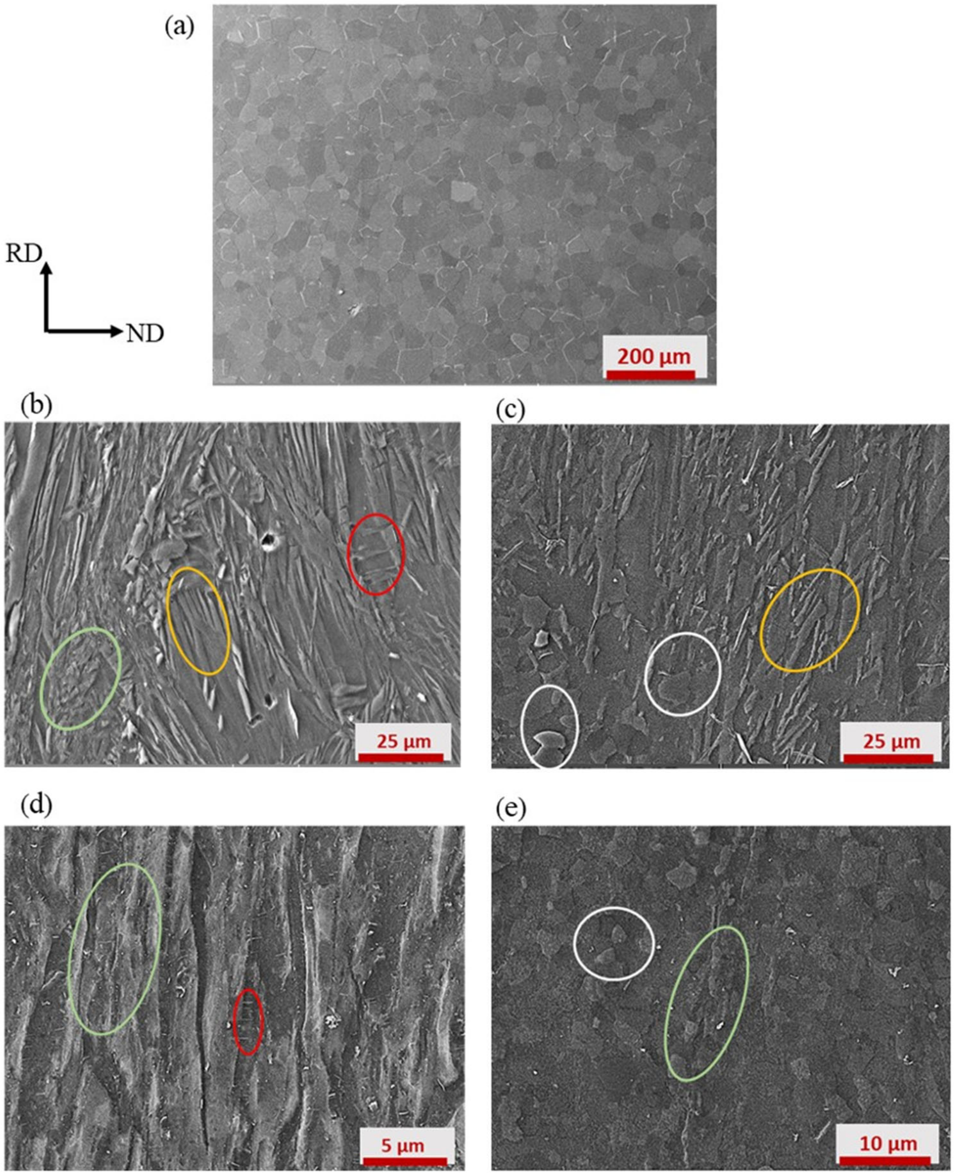

Fig. 1. Scanning electron microstructure of cp-titanium: (a) initial, (b) 50% CR, (c) 50% CR and 90 s annealed at 650°C, (d) 70% CR and (e) 70% CR and 90 s annealed at 650°C, respectively. The yellow circle shows deformation laths, the red circle shows twins, the white circle shows recrystallized grains, and the green circle shows highly deformed regions (Color figure online).

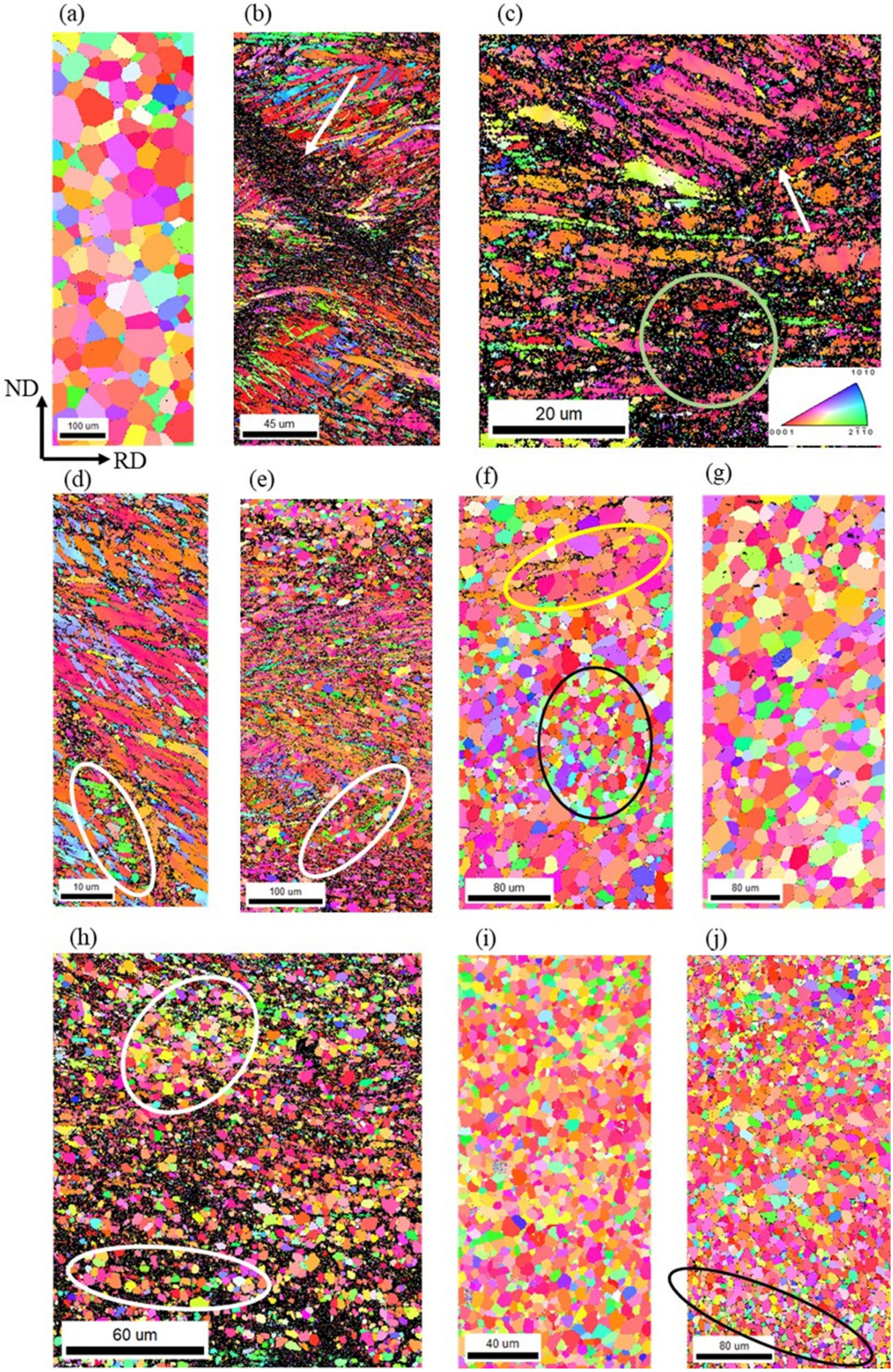
(a)
(b)
(c)
ND
RD
100 um
45 um
20 um
1010
0001
2110
(d)
(e)
(f)
(g)
10 um
100 um
80 um
80 um
(h)
(i)
(j)
60 um
40 um
80 um

◀Fig. 2. Inverse pole figure (IPF) map of cp-titanium: (a) initial, (b) 50% CR, (c) 70% CR, (d) 50% CR 90 s, (e) 50% CR 105 s, (f) 50% CR 180 s, (g) 50% CR 300 s, (h) 70% CR 120 s, (i) 70% CR 180 s and (j) 70% CR 300 s annealed at 650°C, respectively. White arrow shows the shear band, green circle shows the highly deformed region, and white circle shows the recrystallized grains in different regions. Black circled region shows more randomly oriented grains compared to the rest of the regions. The IPF colour coding refers to the direction parallel to ND (Color figure online).

peak intensity at $\{1125\} < 1100 >$ and a weak intense peak at $\{2133\} < 1100 >$ is clearly discernible.

Evolution of Microstructure and Texture During Annealing

Figure 1c and e shows the partially recrystallized SEM micrographs of the 50% CR and 70% CR samples, respectively, after annealing at 650°C for 90 s. In the case of the 50% CR sample, incipient recrystallization is observed. Very few equiaxed recrystallized grains (white circle) can be seen. These grains only originated in highly deformed regions. At this initial stage, the lath region does not get recrystallized. In comparison, in the case of the 70% CR sample, many recrystallized grains can be observed. Faster kinetics of recrystallization in this case is evident because of the high stored energy of deformation. It can also be seen that along certain lines (green circle in Fig. 1e), many very fine grains appeared. This is attributed to a higher nucleation density at the high energy regions such as certain bands or grain boundaries.

Figure 2d–g displays the IPF maps of 50% CR samples after annealing for 90, 105, 180 and 300 s at 650°C, respectively. After 90 s of annealing, along the band (white circle in Fig. 2d) many nuclei with different orientations have formed. Recrystallized grains along the lath appear after 105 s of annealing. These grains are indicated by a white circle in Fig. 2. By contrast, it is interesting to see that in this case the orientations of the recrystallized grains are very similar in colour to the neighbouring lath from which they got nucleated. A detailed account of the mechanism of formation of nuclei with specific orientations will be presented in Sect. 5 in the discussion. After complete recrystallization (180 s of annealing), two completely different regions of recrystallized grains could be seen (Fig. 2f). In the black circle, the orientations of the recrystallized grains are random (i.e., deviating from known texture components); hence, these grains are likely to originate within regions of very high dislocation density.

Grains grouped in the yellow circle have orientations similar to that of the lath. Thus, we assume that their nuclei were formed through subgrain coalescence and that the mechanism of oriented nucleation was activated. The mechanism of the formation of nuclei and its growth will be discussed in detail later in the discussion section. Figure 2g shows grain growth after complete recrystallization. After this stage, a significant increase in the size of grains occurs. Figure 2h–j shows the IPF map of 70% CR samples annealed after 105, 180 and 300 s at 650°C, respectively. Recrystallization kinetics is faster for increasing deformation. Overall, the grain size is smaller in this case because of a higher nucleation density. Similar to the case of 50% CR, some regions of randomly orientated nuclei and some regions of uniform orientation can also be seen (Fig. 2h and j).

Figure 3 shows (0001) pole figures of deformed and recrystallized samples as a function of annealing time. Figure 3c–3 shows the (0001) pole figure of only recrystallized grains for 50% CR samples annealed after 105, 180 and 300 s at 650°C, respectively. After 105 s of annealing (10% RX), most of the orientations are close to the deformed orientations with only deviation of 10–15° misorientation.

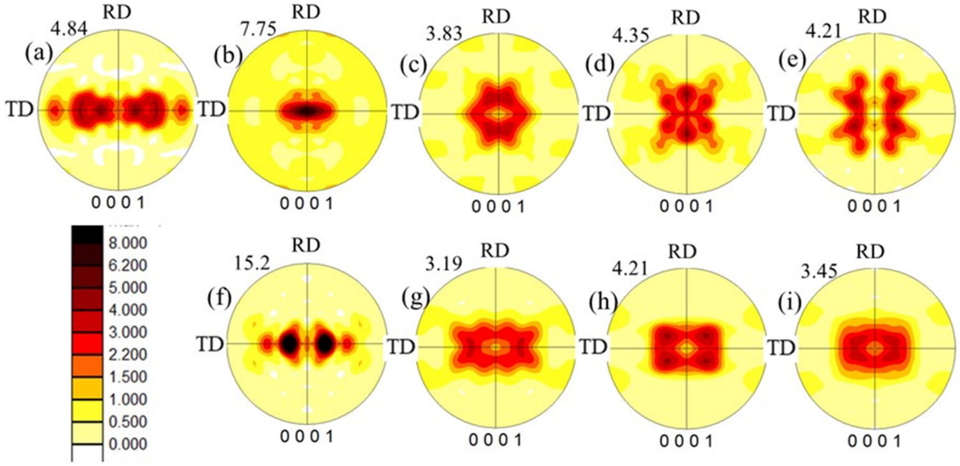

Fig. 3. (0001) Pole figure of (a) initial, (b) 50% CR, (c) 50% CR 105 s (15% RX), (d) 50% CR 180 s (99% RX), (e) 50% CR 300 s (grain growth), (f) 70% CR, (g) 70% CR 90 s (18% RX), (h) 70% CR 180 s (100% RX), (i) 70% CR 300 s (grain growth) and annealed at 650°C, respectively. Annealed sample shows orientation of only recrystallized grains partitioned through TSL OIM8.1 (Color figure online).

This clearly indicates nucleation through subgrain coarsening. However, it shows more spread toward the RD and rather less split across the same direction (TD), about 30° away from the centre. Similar rotations by 30° of the deformed grains during recrystallization of cp-titanium have been reported by many researchers for the TD split deformation texture, i.e., from {2115} < 0110 > to {1013} < 1210 > orientation.[2] After complete recrystallization, the RD split orientation became more intense, and a new component rotated by 30° about the c-axis from nuclei orientations appeared. This suggests that this orientation forms preferentially during the growth of the nuclei in the deformed matrix. The main recrystallization texture components are {1014} < 2131 >, {1013} < 2131 > and {1235} < 2311 > (Fig. 3d). However, the overall texture intensity decreased during recrystallization, which is because of random nucleation in the highly deformed regions as explained above. On further annealing, grain growth occurred and a substantial change in texture is observed during this stage. The {1014} < 2131 > component diminished whereas {1013} < 2131 > and {1235} < 2311 > became stronger.

Figure 3g–i shows the (0001) pole figures generated only from the recrystallized grains of the 70% CR samples subjected to annealing at 650°C for 105, 180 and 300 s, respectively. In this case the orientation of the nuclei was within 10–15° deviation to the deformation texture. This indicates that the mechanism of nucleation is through sub-grain coalescence. However, the orientations of the nuclei are different in 50% and 70% rolled materials. After complete recrystallization, the main texture component formed is {1013} < 3031 >, which is 30° rotated from the deformation texture components (Fig. 3h). One significant difference between the recrystallization texture of 50% and 70% CR samples is that the recrystallization texture is very weak in the 70% CR sample compared to their deformation texture. This is anticipated because more defects are present in this case, such as the presence of shear bands. On further annealing after complete recrystallization, the texture weakens forming a weak fibre 30–40° away from the basal orientation.

Figure 4a shows the misorientation angle profile of a 50% cold-rolled (CR) sample as a function of annealing time. With the progress of annealing, the fraction of grain boundaries with misorientation range 10–25° and 50–60° has increased. The other boundaries do not show a clear trend. There is, however, a large dip corresponding to misorientation angles ~ 33° and 64.3°, which is attributed to the decrease in the number of tensile (34°/ < − 1100 >) and compression (64.3°/< − 1100 >) twins that eventually disappear during recrystallization.

Figure 4b shows the variation in microhardness as a function of annealing time. The 70% CR sample has a higher hardness (230 ± 8 HV) than the 50% CR (195 ± 14 HV) sample. However, for larger annealing times, both samples exhibit similar hardness. The hardness data have also been used to calculate recrystallization kinetics in each case using Eq. 1.

RESULTS OF COMPUTER SIMULATIONS

Critical Parameters

It is necessary to predict the response of a material to plastic deformation and annealing for the simulation of the recrystallization. For this purpose, the grain orientation spread (GOS) values of each grain scaled with an overall dislocation density of the material and a CA were utilized, respectively. The combination with experiments allows both the use of real microstructure information and the validation of the accuracy of the models. The four main parameters had to be accounted for in any quantitative recrystallization microstructure evolution model: (1) the grain size distribution in the deformed state, (2) the local plastic deformation, i.e., strain and orientation gradients, which define the nucleation criteria, (3) the spatial distribution of nucleation sites and (4) whether any special orientation appeared during recrystallization. With respect to the aspect (1), two different deformation levels (50% CR and 70% CR) of microstructures were used from experiments. Besides, homogeneous nucleation in the bulk and heterogeneous nucleation at grain boundaries, transition bands and shear bands were considered. The nucleation was simplified in such a way that the bulk nucleus density was determined from large area EBSD data, whereas the distribution of nuclei on grain boundaries was derived from the mean dislocation densities of the neighbouring grains.

Recrystallization Behaviour

Figure 5a compares simulated recrystallization kinetics with experimental kinetics of recrystallization obtained through micro-hardness data for both levels of deformation. The curve depicting recrystallization kinetics exhibited a sigmoidal shape with 80% recrystallization after annealing for 175 s for the 50% rolled sample and after 150 s for the 70% rolled sample. The simulated curve shows a good match with experiments with slight deviations. The incubation time was found to be a little less in the case of the simulation of 50% CR samples. Once recrystallization started, both experimental and simulated curves rose quickly, and after 50-60% recrystallization, slowed down significantly. The reason behind the slowdown of recrystallization kinetics is the presence of some low stored energy grains in the final stages of recrystallization.[41,42] Overall, the simulated kinetics agrees quite well with the experiments, although recovery was not considered during the simulation. The

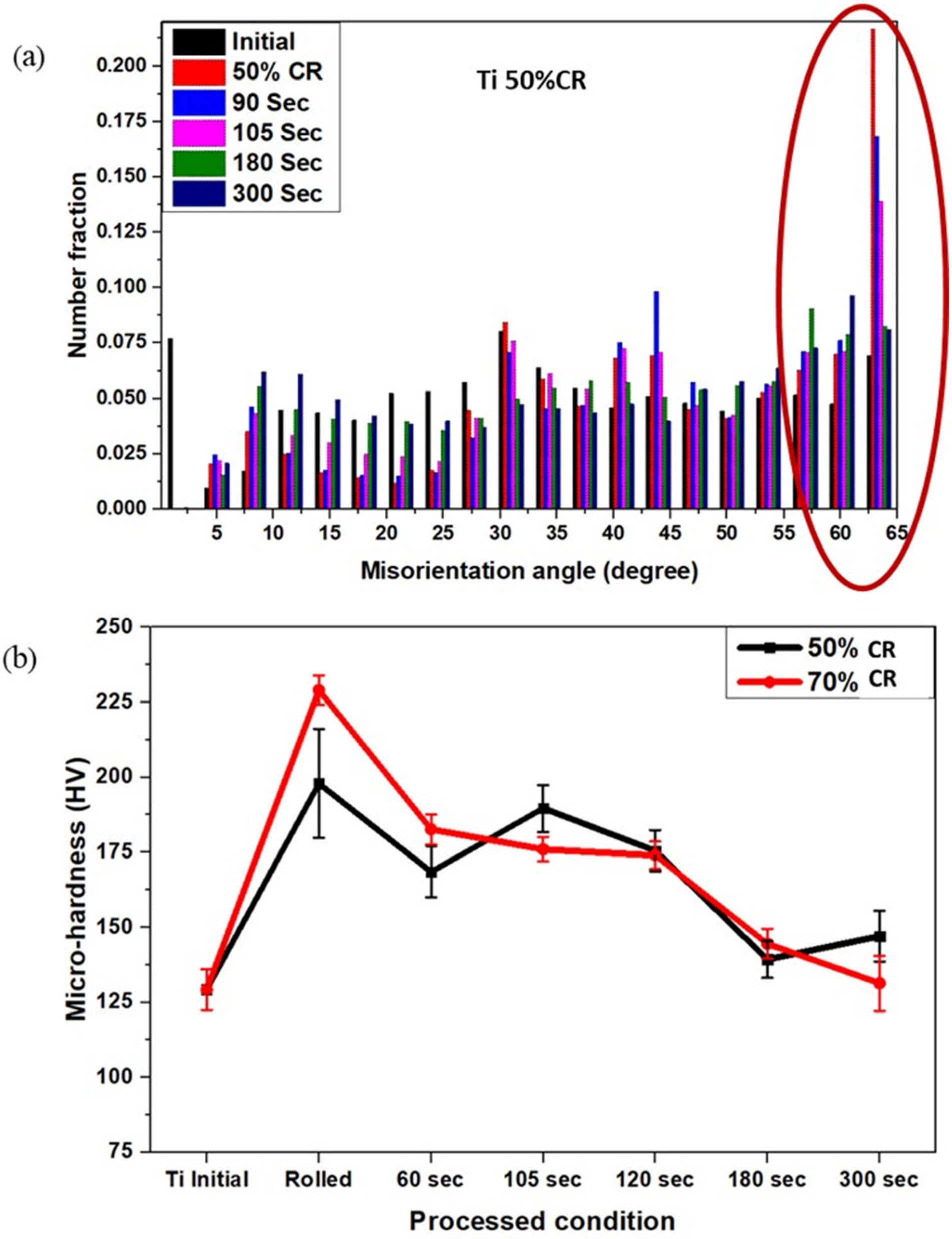

Fig. 4. (a) Misorientation angle distribution of 50% CR cp-titanium as a function of annealing time obtained from EBSD data. (b) Variation of micro-hardness of initial, deformed and annealed samples.

recrystallization kinetics was also interpreted in the context of the classic Johnson–Mehl–Avrami–Kolmogorov (JMAK) model[43,44] in which the recrystallized fraction, X_{RX}, depends on time, t, as follows:

$$X_{RX} = 1 - \exp(-B.t^n) \tag{3}$$

where B is a parameter that depends on the nucleation and growth rates, and n is the Avrami exponent that depends on the nucleation conditions as well as dimensionality of growth. n ranges from 2 to 3, corresponding to site-saturated nucleation and continuous nucleation, respectively, for two-dimensional growth.[43] In Fig. 5b, the experimental data for X_{RX} versus t are re-plotted in the typical manner, i.e., as a JMAK plot, to determine the value of the Avrami exponent n. In case of 50% deformation, the experimental data show two different values of the Avrami exponent are apparent, i.e., 3.9 and 3.1, corresponding to the initial period and the later period, respectively. In case of the sample with 70% deformation, the data show two different values of the Avrami exponent, i.e., 3.3 and 1.9, corresponding to the initial period and the later period of recrystallization, respectively. Such a deviation from the linear JMAK kinetics has been reported in the literature.[45]

Figure 5c shows a comparison of the grain size of the experimental microstructure with the simulated

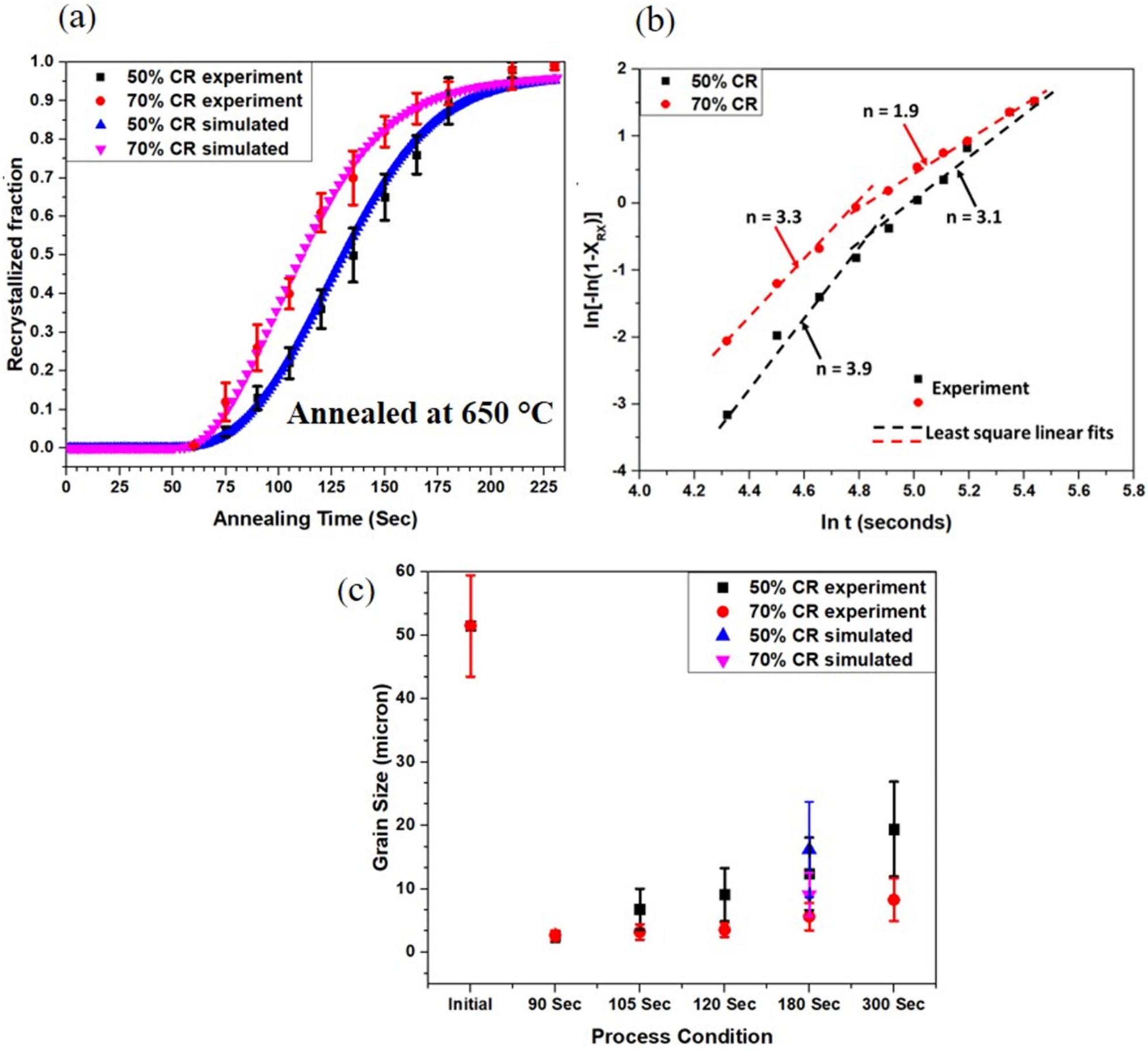

Fig. 5. Comparison of experimental and simulated (a) recrystallization kinetics, (b) JMAK plot of experimental recrystallization kinetics and (c) recrystallized grain size distribution of 50% and 70% rolled samples at different annealing times.

one. It should be noted that, in this measurement, only recrystallized grains were considered. The recrystallized grain size of the 50% CR sample was found to be 12 ± 5 μm and for 70% CR was found to be 6 ± 2 μm through experimental microstructures. CA simulations predict few higher grain sizes in both cases after complete recrystallization. The reason behind this is the faster impingement of nuclei in necklace structures (in lath region) than in arrangements with random spatial distribution. The grain size distributions in the simulation were slightly shifted toward higher mean values.

Figure 6a–p shows the simulated recrystallized microstructure evolution through IPF maps at different levels of recrystallization. The nucleation mechanism obtained through experiments was incorporated in the simulation, i.e., nucleation by subgrain coarsening at grain boundaries, random nucleation at shear bands and uniform distribution of experimental nuclei orientation in bulk nucleation. The shape of the grains also matches well with experiments. Initial grain size distribution input to the simulation and accurate grain boundary mobility are the key factors for precise prediction of recrystallized microstructure and its kinetics. One difference between the simulations and experiments is that necklace formation is more prominent in the experiments, which could be because the probability of nucleation is very sensitive to the difference of dislocation density across a boundary. This indicates that grain boundary nucleation is slightly underestimated in the model.

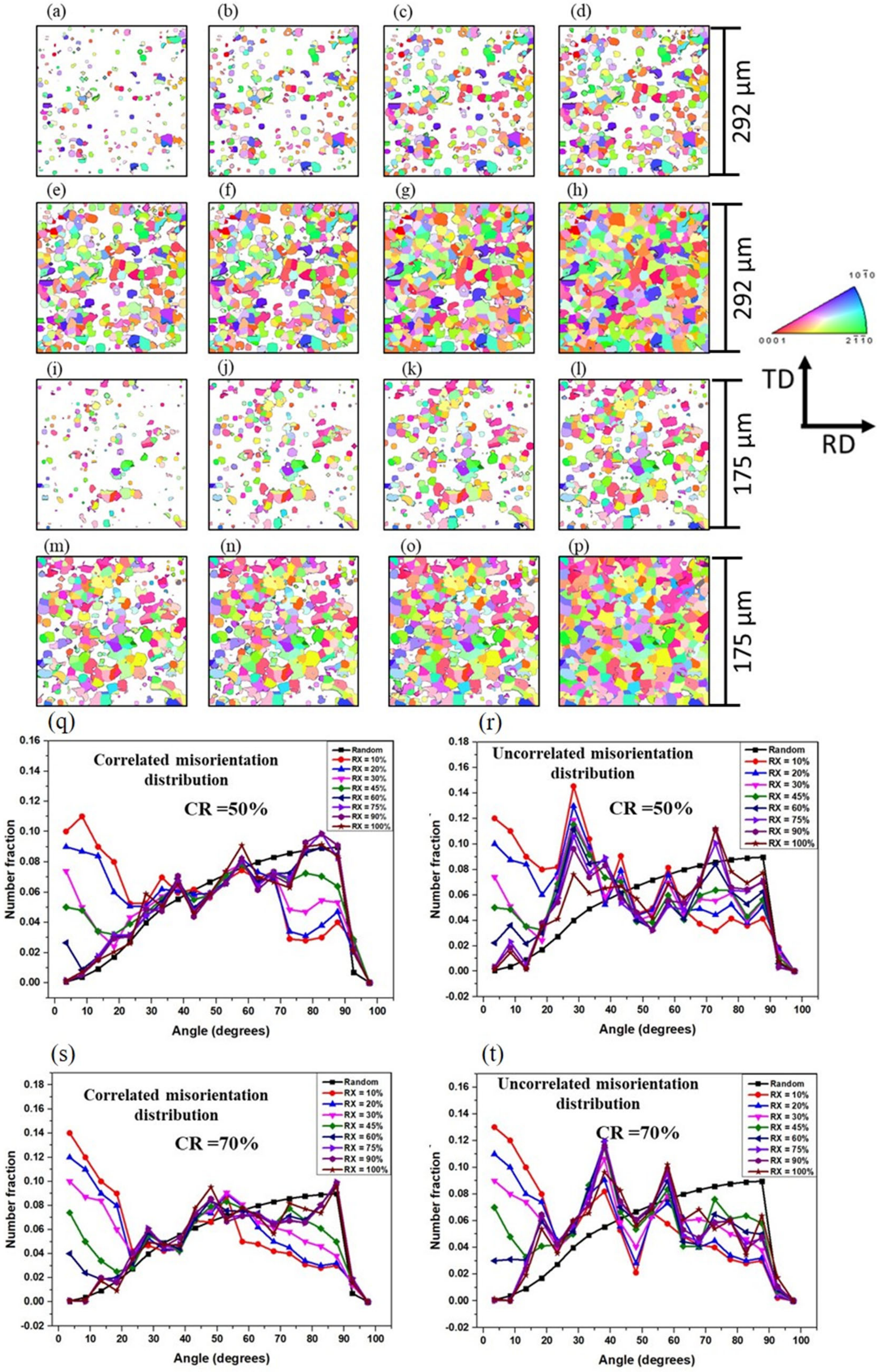
(a)
(b)
(c)
(d)
292 µm
(e)
(f)
(g)
(h)
292 µm
$10\bar{1}0$
0001
$2\bar{1}\bar{1}0$
TD
RD
(i)
(j)
(k)
(l)
175 µm
(m)
(n)
(o)
(p)
175 µm
(q)
Correlated misorientation distribution
CR =50%
Number fraction
Angle (degrees)
Random
RX = 10%
RX = 20%
RX = 30%
RX = 45%
RX = 60%
RX = 75%
RX = 90%
RX = 100%
(r)
Uncorrelated misorientation distribution
CR =50%
Number fraction
Angle (degrees)
(s)
Correlated misorientation distribution
CR =70%
Number fraction
Angle (degrees)
(t)
Uncorrelated misorientation distribution
CR =70%
Number fraction
Angle (degrees)

◀ Fig. 6. Simulated IPF map of 50% deformed and annealed at 650°C: (a) 10%, (b) 20%, (c) 30%, (d) 45%, (e) 60%, (f) 75%, (g) 90%, (h) 100% recrystallized, 70% deformed and annealed at 650°C, (i) 10%, (j) 20%, (k) 30%, (l) 45%, (m) 60%, (n) 75%, (o) 90% and (p) 100% recrystallized samples, respectively. Evolution of misorientation distribution with an increase in the recrystallization fraction for 50% CR (q) correlated misorientation distribution, (r) uncorrelated misorientation distribution; for 70% CR, (s) correlated misorientation distribution, (t) uncorrelated misorientation distribution. In all the cases misorientation distribution is compared to random distribution.

To improve the quality of the simulations a better estimation of the dislocation densities would be needed. This can be done by CP-FEM simulations[46] or a more accurate experimental determination.[47]

Figure 6q–t shows the evolution of correlated and uncorrelated misorientation distributions from simulated recrystallized orientation data for both deformation levels (50% and 70% rolling reduction). The fraction of low-angle misorientation (< 15°) decreases with increases in the degree of recrystallization. Moreover, in both cases, the correlated misorientation distributions are close to random distribution after complete recrystallization. The uncorrelated misorientation distributions show peaks near 30° misorientation for both deformation levels.

Figure 7a and b displays the experimental (0001) pole figures of the 50% CR and 70% CR samples after 180 s annealing (99% RX) measured by x-ray diffraction. The bulk textures in both cases are in agreement with the EBSD measurement. Figure 7c shows the CA simulated pole figure after 100% recrystallization of the 50% CR material. The simulated texture matches well with the experimental texture except for the fact that the simulated texture is relatively stronger. While the simulated texture consists of strong intensities that can be seen at the {1211} < 2112 >, {1233} < 1101 > and {1014} < 2131 > components, the {1014} < 2131 > component is also reasonably strong in the experimental pole figure. The strong simulated texture could be due to an underestimation of nucleation occurring within highly deformed regions of the microstructure. This underestimation would also explain the slight mismatch in grain size. It is well known that nuclei originating within these regions tend to randomize the texture. Figure 7d and e shows the (0001) pole figure of experimental 70% CR and the corresponding sample after 80 s annealing (99% RX) measured by x-ray diffraction. In this case also, the bulk texture is found to be similar to the texture measured by EBSD; the deformed sample shows a strong {1125} < 1100 > component (TD split), whereas the recrystallized sample shows a {1013} < 3031 > texture component. Figure 7f shows the CA simulated recrystallization texture of the 70% CR material. Similar to the previous case, the simulated texture is stronger. However, the intensity maxima at {1013} < 3031 > in the simulated pole figure is in good agreement with the experimental pole figure, which shows 20–30° rotation of the TD split deformed texture component. Other than that, the simulated pole figure also shows a high intensity at {1014} < 2131 > (20° away from the centre towards RD), which is weaker in the experimental pole figure. It is to be mentioned here that no fitting parameters were used for the simulations.

DISCUSSION

Effect of Deformation on the Evolution of Recrystallization Texture

The initial hot-rolled and annealed plate, which is considered as the initial sample, was given two different rolling reductions, namely 50% CR and 70% CR. Table I shows the main texture components and orientation density in different processed conditions. As explained in Sect. 2, the 50% CR sample was characterized by a basal fibre texture having 15–18° spread along the TD and 8–10° spread along the RD, which is not a usual rolling texture of cp-titanium. This is attributed to the relatively low deformation for the 50% CR sample, which was not enough to produce a typical TD split deformation texture. This is confirmed by the fact that after 70% CR, the samples substantiated the expected rolling texture of cp-titanium having a {1125} < 1100 > component.[5] In addition to this component, a minor {2133} < 1100 > component was also found.

For the 50% CR sample, we studied the unexpected recrystallization texture components {1014} < 2131 >, {1013} < 2131 > and {1235} < 2311 >. It is well known that when the rolling textures have a common component such as {1125} < 1100 >, their recrystallization texture is formed by a 30° rotation about the c-axis, i.e., the {1013} < 3031 > component. In this case, the recrystallization mechanism was reported to be subgrain coalescence and discontinuous subgrain coarsening.[6] For 50% CR, the recrystallization texture formed is different from the usual recrystallization texture of cp-titanium. Hence, we can say that recrystallization texture in cp-titanium is very dependent on the initial deformation texture. The main texture components in this case are {1014} < 2131 >, {1013} < 2131 > and {1235} < 2311 >, all having weak intensity. However, it should be noted that all these components are within 20–30° misorientation of the corresponding deformation texture components. This can be explained by substantial occurrence of discontinuous subgrain coarsening and subgrain coalescence, i.e., oriented nucleation. However, some other mechanism must be operating because the weakening of texture during recrystallization is also evident. Recrystallization texture formation can be better explained based on the site of nucleation. The deformed microstructure can be divided as lath areas within the grain, grain boundary regions, highly deformed (regions having very high dislocation density) or shear band regions, and twin interface regions. The recrystallization mechanism in each section will be explained in the next section.

Role of Different Deformation Features on the Nucleation Mechanism

Figure 8 shows some selected regions of IPF superimposed with the IQ map and corresponding the misorientation angle across the recrystallized grains of the Ti50%CR105s annealed sample. Figure 8a shows some recrystallized nuclei within the lath. All of these nuclei formed a necklace-type structure, and their orientations are very close to the orientation of the neighbouring laths. Figure 8b

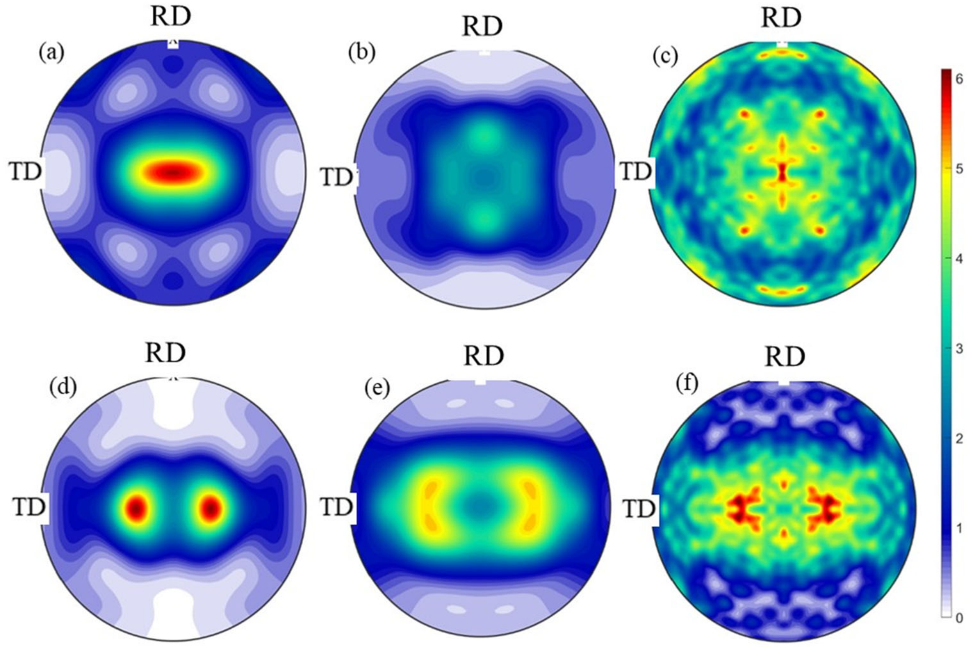

Fig. 7. (0001) Pole figure of (a) experimental 50% CR, (b) experimental 50% CR and 100% recrystallized, (c) simulated 50% CR and 100% recrystallized, (d) experimental 70% CR, (e) experimental 70% CR and 100% recrystallized, and (f) simulated 70% CR and 100% recrystallized samples, respectively.

Table I. Main texture components and orientation densities in different processed conditions

Process	Texture orientation	Orientation density
Hot-rolled and annealed plate (Initial sample)	{0001} < 1230>	4.8
	{1101} < 0110>	3.3
	{3211} < 0110>	3.1
50% cold-rolled (CR)	Basal fibre with 15–18° spread along TD and 8–10° spread along RD	7.75
70% cold-rolled (CR)	{1125} < 1100>	15.2
	{2133} < 1100>	3.3
50% cold-rolled and 100% recrystallized	{1014} < 2131>	4.1
	{1013} < 2131>	3.2
	{1235} < 2311>	2.8
70% cold-rolled and 100% recrystallized	{1013} < 3031>	4.2

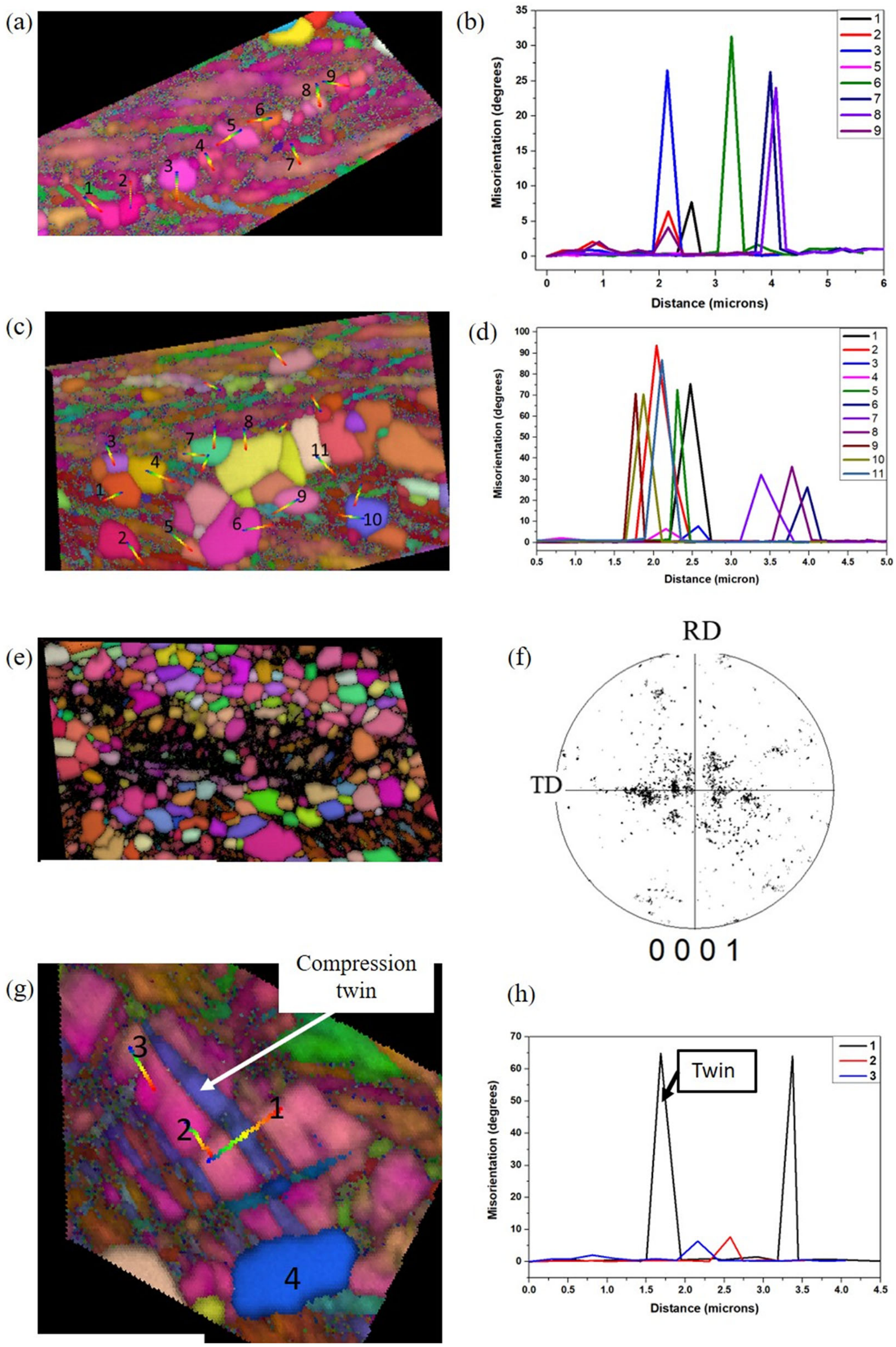

Fig. 8. Some selected regions of IPF superimposed with the IQ map of Ti50%CR105s annealed (a) recrystallized nuclei near the lath region, (b) point-to-point misorientation across nuclei in the lath region, (c) recrystallized nuclei at grain boundaries, (d) point-to-point misorientation across nuclei at the grain boundaries, (e) recrystallized nuclei in the highly deformed region of bands, (f) (0001) pole figure of recrystallized grains in the highly deformed region, (g) recrystallized grain along the twin boundaries and (h) point-to-point misorientation across grains near the twin boundaries.

shows the point-to-point misorientation profile across some of the nuclei. It was found out that most of the new grains are either 7–10° misoriented from their neighbour deformed lath or misoriented by 30°. The former rotation suggests subgrain coarsening, whereas the latter is a typical grain rotation observed during recrystallization of cp-titanium, which suggests the mechanism of subgrain coalescence.[2]

Figure 8c shows some recrystallized nuclei along the grain boundaries. It can be seen that some of the grains are close to the orientation of neighbouring grains. Some grains also have very different orientations from all of their neighbours. Figure 8d shows the point-to-point misorientation profile across all of these nuclei. Some grains are very highly misoriented (50–90°) from their neighbours, suggesting random nucleation, and some grains are also 20–30° misoriented and follow a similar mechanism as on laths.

Figure 8e shows the recrystallization in highly deformed shear band regions, where dislocation density is very high. It shows that indeed nuclei originating from within these regions tend to be randomly oriented as plotted on the (0001) pole figure (Fig. 8f). Figure 8g shows recrystallization along the twin interface. It shows a compression twin of $64.3^\circ/< -1100 >$ type (1 in Fig. 8h) and the formation of recrystallization nuclei in its neighbour grain. Here, recrystallization proceeds along the interface of twin boundaries where the lath is subdivided and misorientation across this division is 8° (2 in Fig. 8h) and 7° (3 in Fig. 8h). This implies the operation of the mechanism of subgrain coarsening along the twin boundary interface. One nucleus (grain 4) was also found to nucleate at the triple point, where the twin boundary ends, with an orientation close to that of the twinned region.

CONCLUSION

The recrystallization behaviour of 50% and 70% cold-rolled cp-titanium was investigated by experiments and simulations. A parallel 3D CA model for recrystallization was employed to simulate the recrystallization behaviour. Meticulous experimental studies were done to supply the necessary input data and validate the obtained simulation results. The following conclusions can be drawn:

- The recrystallization texture in cp-titanium depends on the initial deformation texture. The resulting texture is characterized in the 50% CR sample by weak $\{1014\} < 2131 >$, $\{1013\} < 2131 >$, $\{1235\} < 2311 >$ components. In the 70% CR sample, the main texture component is $\{1013\} < 3031 >$.
- CA simulation results show an excellent agreement with kinetics, recrystallized grain size, microstructure and texture. However, the simulated texture is more intense than the experimental texture. This is attributed to an underestimation of nucleation within regions of high dislocation density such as deformation and shear bands.
- In both cases of deformation, the correlated misorientation distributions are close to random distribution after complete recrystallization.
- The mechanism of recrystallization depends on the site of nucleation, suggesting subgrain coarsening in the deformed lath region and random nucleation in highly deformed regions.

ACKNOWLEDGEMENTS

The authors acknowledge the extensive use of the microscopy facilities at the Advanced Facility for Microscopy and Microanalysis (AFMM), Supercomputer Education and Research Centre (SERC), for providing computational facility at the Indian Institute of Science, Bangalore. LABM acknowledges the support of the Indian Institute of Science through the Huber Aaronson Visiting Scientist Fellowship.

CONFLICT OF INTEREST

On behalf of all authors, the corresponding author states that there is no conflict of interest.

REFERENCES

1. F. Wagner, N. Bozzolo, O. Van Landuyt, and T. Grosdidier, *Acta Mater.* 50, 1245 (2002).
2. N. Bozzolo, N. Dewobroto, T. Grosdidier, and F. Wagner, *Mater. Sci. Eng. A* 397, 346 (2005).
3. H.T. Jiang, J.X. Liu, Z.L. Mi, A.M. Zhao, and Y.J. Bi, *Int. J. Miner. Metall. Mater.* 19, 530 (2012).
4. Z.S. Zhu, J.L. Gu, and N.P. Chen, *Scr. Metall.* 30, 605 (1994).
5. N.P. Gurao, R. Kapoor, and S. Suwas, *Acta Mater.* 59, 3441 (2011).
6. C.J. Mchargue, S.E. Adair Jr., and J.P. Hammond, *Trans. AIME* 197, 1149 (1953).
7. S. Naka, R. Penelle, R. Valle and P. Lacombe, in: G. Gottstein and K. Lücke (Eds.), *Proc. 5th Conf. on Texture of Materials, Springer Verlag,* Berlin 1, 405 (1978).
8. S. Naka, R. Penelle, R. Valle and P. Lacombe, in: H. Kimura and O. Izumi (Eds.), *Titanium 80: Science and Technology, AIME, Warrendale, PA,* 955 (1980).
9. M. Blicharski, S. Nourbakhsh, and J. Nutting, *Met. Sci. J.* 13, 516 (1979).
10. H. Inoue and N. Inakazu, in: J.S. Kallend, G. Gottstein (Eds.), *Proc. 8th Int. Conf. on Texture of Materials (ICOTOM-8), The Metallurgical Society, Warrendale, PA, USA,* 997 (1988).
11. S. Nourbakhsh, M. Blicharski and J. Nutting, in: G. Lütjering, U. Zwicker and W. Bunk (Eds.), *Titanium Science and Technology,* DGM Verlagsges, Oberursel, 1729 (1984).
12. H.J. Bunge and C.U. Nauer-Gerhardt, in: G Lütjering, U. Zwicker and W. Bunk. (Eds.), *Titanium Science and Technology*, DGM Verlagsges, Oberursel, 1713 (1984).
13. H. Inagaki, *Z. Metallkunde* 83, 40 (1992).
14. A.K. Singh and R.A. Schwarzer, *Z. Metallkunde* 91, 702 (2000).
15. S.K. Sahoo, R.K. Sabat, S. Sahini, and S. Suwas, *Mater. Des.* 91, 58 (2016).
16. A.W. Bowen, *Mater. Sci. Eng.* 29, 19 (1977).

17. N. Bozzolo, N. Dewobroto, H.R. Wenk, and F. Wagner, *J. Mater. Sci.* 42, 2405 (2007).
18. R.J. Contieri, M. Zanotello, and R. Caram, *Mater. Sci. Eng. A* 527, 3994 (2010).
19. A. Hayama and H. Sandim, *Mater. Sci. Eng. A* 418, 182 (2006).
20. B. Sander and D. Raabe, *Mater. Sci. Eng. A* 479, 236 (2008).
21. G. Shankar, and S. Suwas, *I.O.P. Conf Ser. Mater. Sci. Eng.* 375, 012018 (2018).
22. Z.P. Zeng, S. Jonsson, and H.J. Roven, *Acta Mater.* 57, 5822 (2009).
23. Z.S. Zhu, J.L. Gu, and N.P. Chen, *Scr. Metall.* 34, 1281 (1996).
24. A.K. Singh and R.A. Schwarzer, *Trans. Ind. Inst. Met.* 61, 371 (2008).
25. Z. Zhu, R. Liu, M. Yan, C. Cao, and J. Gu, *J. Mater.* 2, 5163 (1997).
26. H. Inoue and N. Inakazu, in: Chandra T (Ed.), *Recrystallization 90, The Minerals, Metals and Materials Society*, Warrendale, PA, 687 (1990).
27. S.K. Sahoo, R.K. Sabat, B.D. Bishoyi, A.G.S. Anjani, and S. Suwas, *Mater. Lett.* 180, 166 (2016).
28. S.P. Gentry, and K. Thornton, *I.O.P. Conf, Ser. Mater. Sci. Eng.* 89, 012024 (2015).
29. L.A. Barrales-Mora, V. Mohles, P.J. Konijnenberg, and D.A. Molodov, *Comput. Mater. Sci.* 39, 160 (2007).
30. Y.B. Chun, S.L. Semiatin, and S.K. Hwang, *Acta Mater.* 54, 3673 (2006).
31. R.J. Contieri, M. Zanotello, and R. Caram, *Mater. Res.* 20, 688 (2017).
32. R. Hielscher and H. Schaeben, *J. Appl. Crystallogr.* 41, 1024 (2008).
33. F. Bachmann, R. Hielscher, and H. Schaeben, *Solid State Phenom.* 160, 63 (2010).
34. F. Bachmann, R. Hielscher, and H. Schaeben, *Ultramicroscopy* 111, 1720 (2011).
35. C. Haase, M. Kühbach, L.A. Barrales-Mora, S.L. Wong, F. Roters, D.A. Molodov, and G. Gottstein, *Acta Mater.* 100, 155 (2015).
36. M. Kühbach, L.A. Barrales-Mora, and G. Gottstein, *Modell. Simul. Mater. Sci. Eng.* 22, 075016 (2014).
37. M. Kühbach, G. Gottstein, and L.A. Barrales-Mora, *Acta Mater.* 107, 366 (2016).
38. T. Seymour, P. Frankel, L. Balogh, T. Ungár, S.P. Thompson, D. Jädernäs, J. Romero, L. Hallstadius, M.R. Daymond, G. Ribárikch, and M. Preuss, *Acta Mater.* 126, 102 (2017).
39. D.A. Molodov, C. Bollmann, and G. Gottstein, *Mater. Sci. Eng. A* 467, 71 (2007).
40. D.A. Molodov, P.J. Konijnenberg, N. Bozzolo, and A.D. Sheikh-Ali, *Mater. Lett.* 59, 3209 (2005).
41. A.D. Rollett, D.J. Srolovitz, R.D. Doherty, and M.P. Anderson, *Acta Metall.* 37, 627 (1989).
42. H.W. Hesselbarth, L. Kaps, and F. Haessner, *Mater. Sci. Forum* 317, 113 (1993).
43. W.A. Johnson and R.F. Mehl, *Trans AIME.* 135, 416 (1939).
44. P. Gordon and R.A. Vandermeer, *Trans Metall Soc AIME.* 224, 917 (1962).
45. A. Rosen, M.S. Burton, and G.V. Smith, *Trans Metall Soc AIME.* 230, 205 (1964).
46. A. Ma and F. Roters, *Acta Mater.* 52, 3603 (2004).
47. B. Peeters, M. Seefeldt, S.R. Kalidindi, P. Van Houtte, and E. Aernoudt, *Mater. Sci. Eng. A* 319, 188 (2001).

Publisher's Note Springer Nature remains neutral with regard to jurisdictional claims in published maps and institutional affiliations.